NANO LETTERS

pubs.acs.org/NanoLett Letter

# Thickness-Driven Modification of Interface States and Polarization Switching in $MoTe_2/BaTiO_3$ Heterostructures

Yuqing Zhou, Feiyan Hou, Xingke Fu, Chen Ge, Ming Xu,* Kaiming Wang, Siqing Zhang, Jianpei Xing, Li Sun, Ruidong Lv, Qian Liu, Fengjuan Wang, Kaiyang Zeng, Tai Min, and Tao Li*

Cite This: Nano Lett. 2026, 26, 2493−2501

Read Online

ACCESS | Metrics & More | Article Recommendations | Supporting Information

**ABSTRACT:** Van der Waals (vdW) ferroelectric heterostructures provide a versatile platform for exploring interfacial interactions and advanced functionalities. Here, we report a thickness-engineered strategy to modulate the interfacial states and polarization switching in 2H-$MoTe_2/BaTiO_3$ (BTO) heterostructures. The interplay among band-alignment-induced charge transfer, polarization field, and defect-related traps governs the interfacial electronic structure. Remarkably, a two-unit-cell (u.c.) thickness variation (from 18 to 20 u.c.) in $MoTe_2$ induces a 0.44 eV work function shift, reversing the band alignments and interfacial doping polarity. This transition triggers a reversal of BTO polarization from $P_{up}$ to $P_{down}$ state, enabling deterministic and nondestructive polarization control. Electrical transport evolves from trap-assisted space-charge-limited conduction and thermionic emission to Fowler−Nordheim tunneling under strong polarization field, yielding robust multilevel nonvolatile memory characteristics. These results highlight thickness-controlled interfacial states as an effective route to tailor ferroelectric switching dynamics for nonvolatile memory and neuromorphic computing applications.

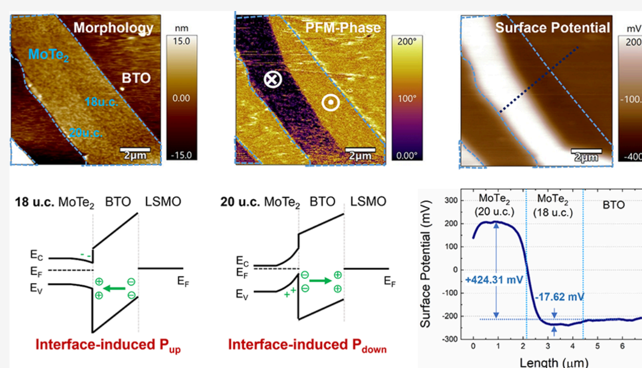


**KEYWORDS:** *TMD/ferroelectric heterostructure, thickness modulation, interface effect, polarization switching, multistate memory*

## 1. INTRODUCTION

Van der Waals (vdW) heterostructures enable bond-free integration that is inherently immune to lattice mismatch and processing constraints, opening new routes for high-performance (opto)electronic devices with diverse functionalities. They feature atomically sharp interfaces, tunable band structures, and excellent electrical conductivity.[1,2] When a transition metal dichalcogenide (TMD) is coupled with a ferroelectric film, the ferroelectric polarization offers a nonvolatile electric field to modulate the charge in the TMD, acting as a polarization field. The nanoscale domain patterning further enables local tuning of its electronic and optical properties. Conversely, the band structure and dielectric screening of the TMD layer critically affect the symmetry and stability of ferroelectric switching. Through the interplay of band-alignment-induced charge transfer, polarization doping, and defect-mediated states,[3−5] rich physical phenomena emerge, including moiré interfacial ferroelectricity,[6,7,9] 2D superconductivity and topological states,[10,11] polar vortices,[12,13] valley polarization,[14−16] tunable exciton emission,[17,18] and fatigue-free ferroelectricity.[19] These effects have enabled diverse device functionalities, such as high-density memory,[3,8,20] neuromorphic computing,[3,21−23] reconfigurable diodes,[1,24] photodetectors,[25,26] optical filtering,[27] and multi-functional in-memory sensors.[10,28] Collectively, these findings establish charge-mediated interfacial coupling in TMD/ferroelectric heterostructures as a versatile strategy to tailor their physical properties and realize multifunctional device applications.

Interfacial interactions in heterostructures are commonly tuned through band-alignment engineering[4,25,29] and electrostatic doping via external and local electric fields.[5,30,31] Exploiting the thickness-dependent band structure of TMDs offers a convenient, nondestructive strategy to modulate these interactions.[2] However, most thickness-dependent studies have focused on monolayer, few-layer, or bulk TMDs due to first-principles scaling limitations, leaving multilayer films comparatively unexplored.[32−34] Despite extensive investigations of TMD/ferroelectric interfaces, the effects of thickness-dependent interfacial coupling and the emergence of reversed interfacial doping have still not been well elucidated. Here,

Received: November 12, 2025
Revised: February 5, 2026
Accepted: February 6, 2026
Published: February 11, 2026

Downloaded via XI'AN JIAOTONG UNIV on March 24, 2026 at 01:19:18 (UTC).
See https://pubs.acs.org/sharingguidelines for options on how to legitimately share published articles.

ACS Publications © 2026 American Chemical Society



https://doi.org/10.1021/acs.nanolett.5c05685
Nano Lett. 2026, 26, 2493−2501

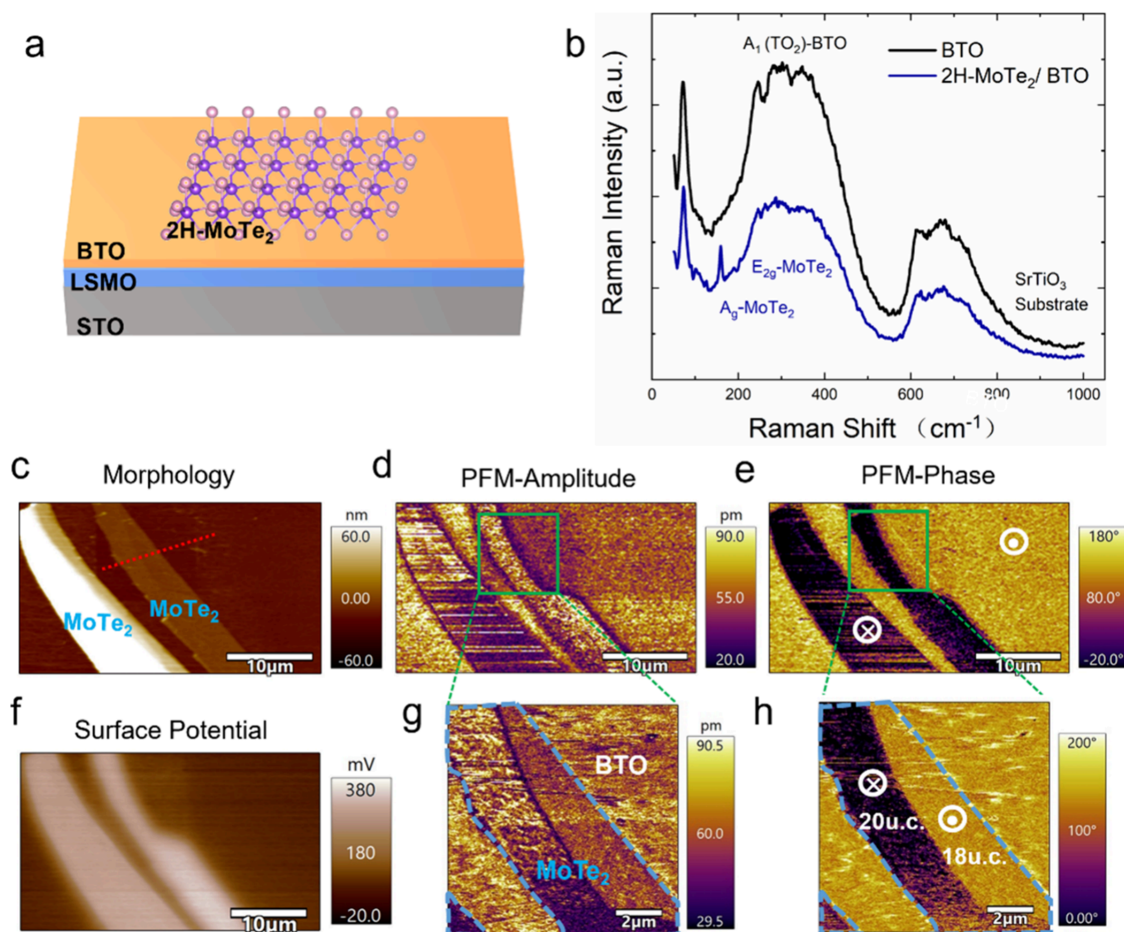


**Figure 1.** Ferroelectric characteristics of the $MoTe_2$/BTO/LSMO heterostructure. (a) Structure schematics of the heterostructure. (b) Raman spectra measured on bare BTO and the $MoTe_2$/BTO/LSMO heterostructure. (c) Morphology, (d) PFM amplitude, (e) PFM phase, and (f) KPFM surface potential images of the $MoTe_2$/BTO/LSMO heterostructure. Zoomed-in (g) PFM amplitude and (h) PFM phase images corresponding to panels d and e.

we systematically investigate thickness-driven interfacial states in TMD/ferroelectric heterostructures by combining in situ scanning probe microscopy (SPM) with COMSOL multiphysics simulations. The study explicitly considers interfacial states arising from polarization doping, band-alignment-induced charge transfer, and defect-related traps.

In this work, we present a thickness-engineered approach that utilizes 2H-$MoTe_2$ with varying thickness to modulate interfacial states in the $MoTe_2$/$BaTiO_3$ (BTO) heterostructure. A large work function difference (0.44 eV) can be induced by 2 u.c. thickness variation (from 18 u.c. to 20 u.c.), inverting the interfacial band alignment and the interfacial doping. This transition drives the ferroelectric polarization switching of the BTO layer from $P_{up}$ to $P_{down}$ state, providing a simple, effective, and nondestructive means to control the interface states and polarization orientation. Favorable band alignment and enhanced interfacial screening in $MoTe_2$ (20 u.c.)/BTO yield symmetric switching with a reduced coercive bias, whereas $MoTe_2$ (18 u.c.)/BTO exhibits asymmetric switching with a higher coercive bias. Electrical transport analyses reveal a transition from trap-assisted space-charge-limited conduction (SCLC) and thermionic emission to Fowler−Nordheim (F−N) tunneling under a strong polarization field in the $MoTe_2$ (20 u.c.)/BTO heterostructure. The interfacial states, arising from polarization field, band-alignment-driven charge transfer, and defect-related states, govern the interfacial carrier distributions and ferroelectric switching dynamics, enabling nonvolatile memory operation. These results experimentally validate thickness-controlled tuning of band alignments and interfacial states in a TMD/ferroelectric stacked heterojunction, establishing an effective and nondestructive strategy for polarization control and paving the way toward interface-tunable 2D memories, reconfigurable logic, and neuromorphic computing.

## 2. RESULTS AND DISCUSSION

Figure 1a shows a schematic of the $MoTe_2$/BTO/LSMO heterostructure. Raman spectra confirm that the $MoTe_2$ film maintains its semiconducting 2H phase (Figure 1b). The morphology in Figure 1c reveals adjacent thick and thin $MoTe_2$ regions, and the height profile indicates that the thin $MoTe_2$ layer consists of two distinct thicknesses of 13.06 (18 u.c.) and 14.70 nm (20 u.c.) (Figure S1a). The associated ferroelectric characteristics and surface potential are characterized by piezoelectricity force microscopy (PFM) and Kelvin probe force microscopy (KPFM). In PFM measurements, an AC bias excites the inverse piezoelectric effect, allowing the detection of the signals of the PFM amplitude (reflecting the piezoresponse strength) and PFM phase (indicating the relative polarization orientation). The region covered by a 20 u.c. $MoTe_2$ layer exhibits a stronger piezo-response than that with 18 u.c. $MoTe_2$ (Figure 1d). Both as-grown BTO and


https://doi.org/10.1021/acs.nanolett.5c05685
Nano Lett. 2026, 26, 2493−2501

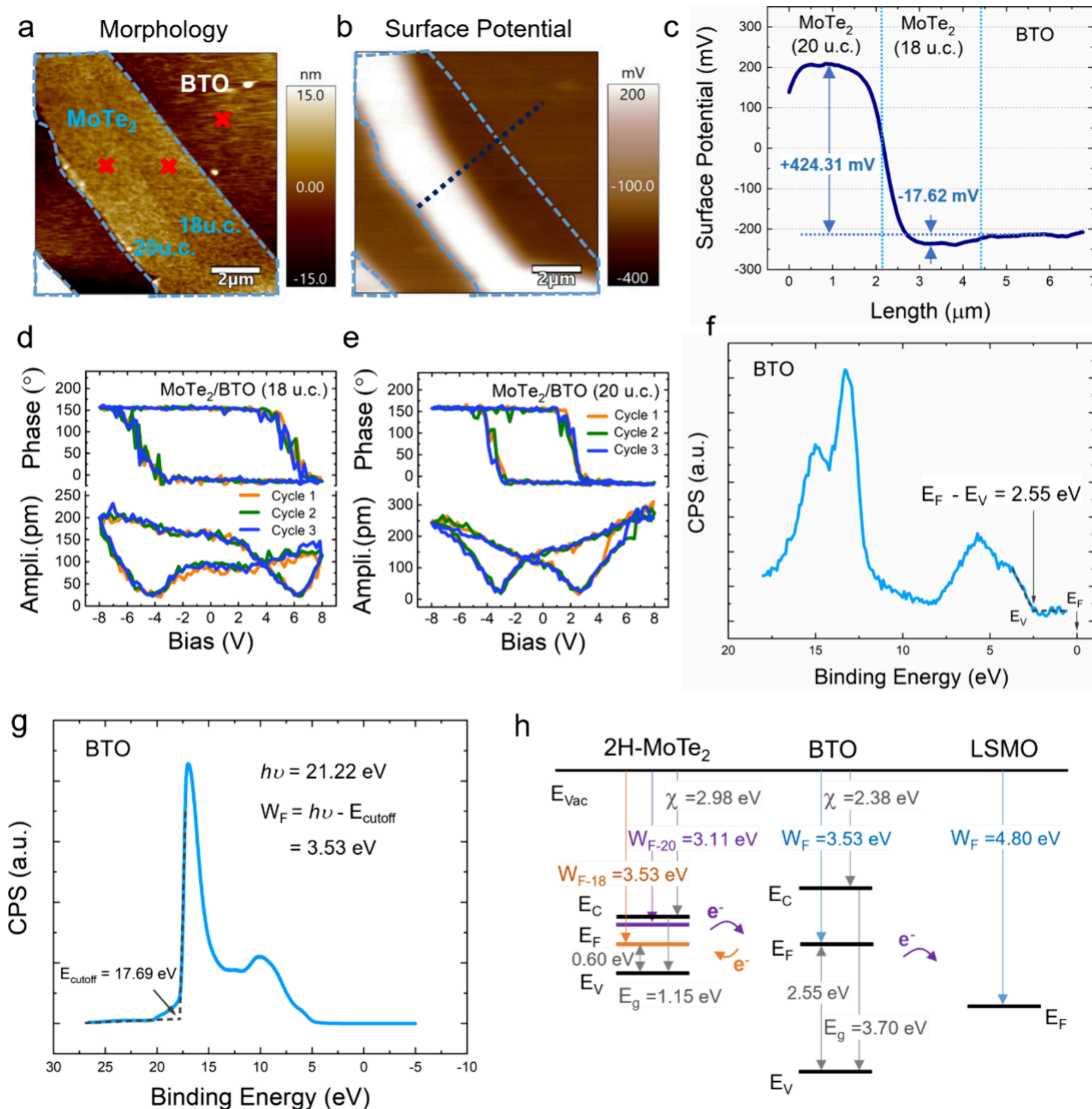


**Figure 2.** Thickness-dependent polarization switching and band alignments of the $MoTe_2$/BTO/LSMO heterostructure. (a) Morphology of the zoomed-in region of the $MoTe_2$/BTO/LSMO heterostructure in Figure 1g,h. (b) Corresponding KPFM surface potential and (c) its line profile along the dark blue-dotted line in panel b. Three-cycle PFM amplitude and phase hysteresis loops measured at the position of the (d) 18 u.c. $MoTe_2$/BTO/LSMO heterostructure and (e) 20 u.c. $MoTe_2$/BTO/LSMO heterostructure (test positions marked by the red crosses in panel a). (f) XPS spectrum and (g) UPS spectrum of the bare BTO film. The intensity is plotted in counts per second (CPS). (h) Illustration of band parameters of $MoTe_2$, BTO, and LSMO layers. $E_{Vac}$, $E_C$, $E_F$, and $E_V$ denote the vacuum band level, conduction band minimum, Fermi level, and valence band maximum, respectively. $W_{F\text{-}18}$ and $W_{F\text{-}20}$ indicate work functions of 18 and 20 u.c. $MoTe_2$. $\chi$ is the affinity. $E_g$ is band gap. The $W_F$ and $E_V$ of BTO are obtained via UPS and XPS, and $W_F$ of $MoTe_2$ is obtained from KPFM. $E_V$ and $E_g$ of the $MoTe_2$ layer are obtained from XPS and PL,[35,36] $E_g$ of BTO is obtained from PL,[36] and $W_F$ of LSMO is obtained from the UPS test.[37]

$MoTe_2$ (18 u.c.)/BTO regions exhibit $P_{up}$ state polarization (pointing away from the LSMO layer), whereas the polarization of the $MoTe_2$ (20 u.c.)/BTO region switches to the $P_{down}$ state (pointing toward the LSMO layer) with an increased surface potential ($V_{sp}$) (Figure 1e and f). The zoomed-in images clearly show that, despite only a 2 u.c. difference, the two regions possess opposite polarization orientations and distinct piezoresponses (Figure 1g and h).

To elucidate the thickness-dependent ferroelectric switching and interface states, detailed analyses of the ferroelectric hysteresis loop and band alignments are presented in Figure 2. During PFM hysteresis measurements, a DC bias applied to the probe tip reverses the polarization, and the corresponding PFM amplitude and phase responses are recorded (bias sequence in Figure S2). The imprint, defined as $(V_{c+} + V_{c-})/2$, represents the loop lateral shift and suggests the interfacial

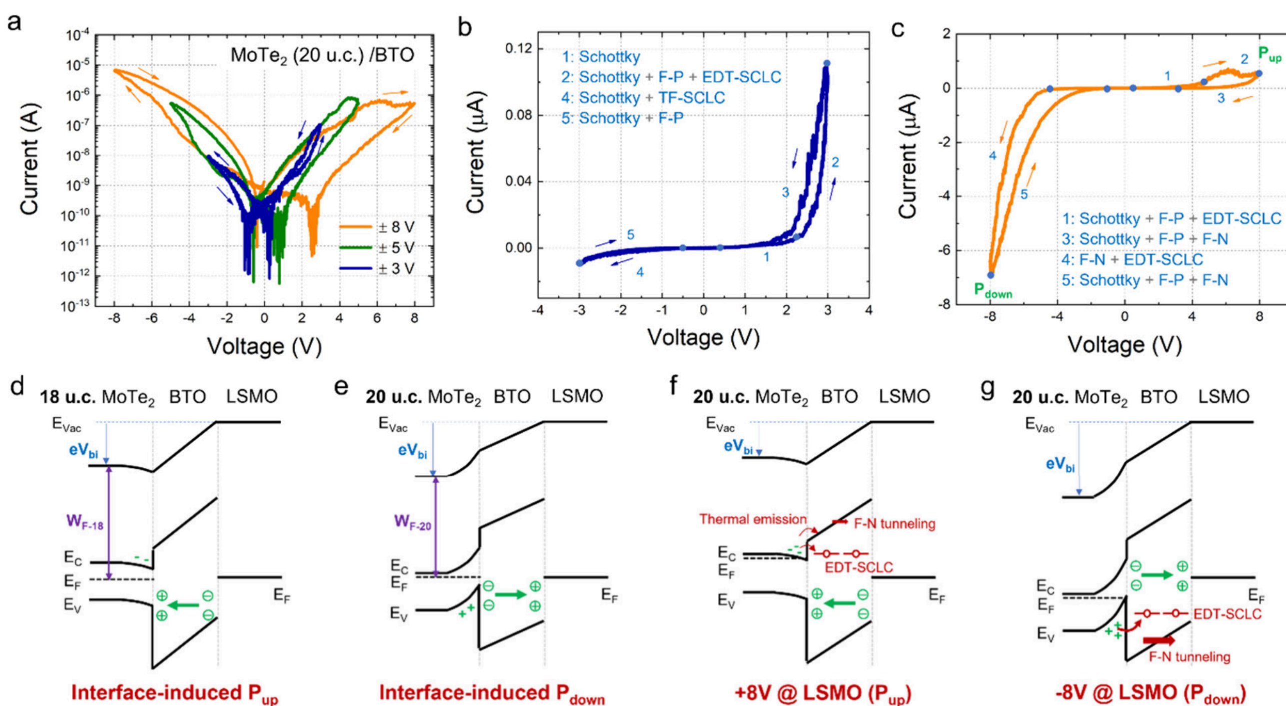


**Figure 3.** Electrical transport characteristics and band structure of the 20 u.c. $MoTe_2$/BTO/LSMO heterostructure. (a) Vertical $I-V$ curves measured under different voltage sweep ranges. Vertical $I-V$ curves (b) under a ±3 V sweeping bias and (c) under a ±8 V sweeping bias, with fitted conduction mechanisms. Schematics of the ideal band structure (d) for $MoTe_2$(18 u.c.)/BTO/LSMO and (e) for $MoTe_2$(20 u.c.)/BTO/LSMO heterostructures. Schematics of the excited-state band structures of $MoTe_2$(20 u.c.)/BTO/LSMO (f) upon applying a +8 V bias on the LSMO film to switch the polarization of BTO to the $P_{up}$ state and (g) upon applying a −8 V bias on the LSMO film to switch the polarization of BTO to the $P_{down}$ state.

built-in field, where $V_{c+}$ and $V_{c-}$ denote the positive and negative coercive biases, respectively. Three-cycle switching spectroscopy PFM hysteresis loops are acquired on bare BTO, 18 u.c. $MoTe_2$, and 20 u.c. $MoTe_2$ regions (marked by red crosses in Figure 2a), demonstrating a high cycling stability. The bare BTO film exhibits symmetric polarization switching with a slight positive imprint ($V_{c-}/V_{c+}$: −1.70/+1.90 V, Figure S1b). In contrast, the $MoTe_2$(18 u.c.)/BTO heterostructure shows an asymmetric hysteresis loop with stronger piezo-response under negative bias and larger positive coercive voltage (−4.95/+6.25 V), indicating a positive imprint and a strong interfacial field stabilizing the $P_{up}$ state (Figure 2d). The $MoTe_2$(20 u.c.)/BTO heterostructure exhibits symmetry piezo-response and slight negative imprint ($V_{c-}/V_{c+}$: −3.05/+2.95 V), demonstrating easier polarization reversal and weaker domain pinning (Figure 2e). To confirm the stability of this thickness-dependent polarization switching, an additional $MoTe_2$/BTO/LSMO heterostructure was fabricated (Figure S3). The 8 u.c./18 u.c. $MoTe_2$ layer exhibits $P_{up}$ state polarization, while the 30 u.c. $MoTe_2$ layer shows $P_{down}$ state polarization (Figure S3a−c). Corresponding KPFM mapping shows $V_{sp}$ comparable to bare BTO for the 8 and 18 u.c. samples and a pronounced enhancement for the 30 u.c. $MoTe_2$/BTO region (Figure S 3d). The hysteresis switching characteristics are also consistent with those in Figure 2d and e (Figure S3f and g).

To quantitatively determine the band alignment of the $MoTe_2$/BTO/LSMO heterostructures, the band parameters of the BTO film are extracted from X-ray photoelectron spectroscopy (XPS) and ultraviolet photoelectron spectroscopy (UPS) measurements. The work function ($W_F$) of BTO is 3.53 eV from the secondary electron cutoff energy in the UPS spectrum (Figure 2g), and the valence band maximum ($E_V$) is 6.08 eV based on a 2.55 eV separation between the Fermi level and $E_V$ in the XPS spectrum (Figure 2f). In KPFM measurements, $V_{sp}$ is defined as $(\phi_{tip} - \phi_{sample})/e$, where $\phi_{tip}$ and $\phi_{sample}$ represent $W_F$ of the conductive tip and sample, respectively, and $e$ is the elementary charge. Accordingly, an increase in $V_{sp}$ corresponds to a lower sample $W_F$ (upward Fermi-level shift) and reduced electrostatic potential. As shown in Figure 2b and c, the 20 u.c. $MoTe_2$ region exhibits a 424.31 mV increase in $V_{sp}$ relative to BTO, whereas the 18 u.c. $MoTe_2$ region shows a slight decrease of 17.62 mV. These band alignments arise from the polarization field and the pristine $W_F$ alignment. To quantify their contributions, the $V_{sp}$ of $MoTe_2$ films with different thicknesses on the $SiO_2$ substrate is measured (Figure S4). The $V_{sp}$ difference of 121.69 mV was observed between thinner and thicker $MoTe_2$ films, with thicker $MoTe_2$ exhibiting a higher $V_{sp}$. As for the $V_{sp}$ difference between thinner $MoTe_2$ and BTO, several tens of millivolts with a downward shift are observed on various $MoTe_2$/BTO heterostructures (Figures 2b and S3d). These results indicate that despite the relatively small pristine thickness-dependent $V_{sp}$ variation, the opposite $V_{sp}$ alignment of $MoTe_2$ with different thicknesses relative to BTO reverses charge-transfer characteristics and polarization preference, thereby enabling polarization switching in the 20 u.c. $MoTe_2$/BTO heterostructure and the pronounced $V_{sp}$ enhancement of 441.93 mV. All of the band parameters of the $MoTe_2$/BTO/LSMO heterostructures are summarized in Figure 2h, revealing the opposite band alignments for $MoTe_2$ (20 u.c.)/BTO and $MoTe_2$ (18 u.c.)/BTO interfaces.

Based on the aforementioned thickness-dependent polarization characteristics, the $MoTe_2$ (≥20 u.c.)/BTO/LSMO


https://doi.org/10.1021/acs.nanolett.5c05685
Nano Lett. 2026, 26, 2493−2501

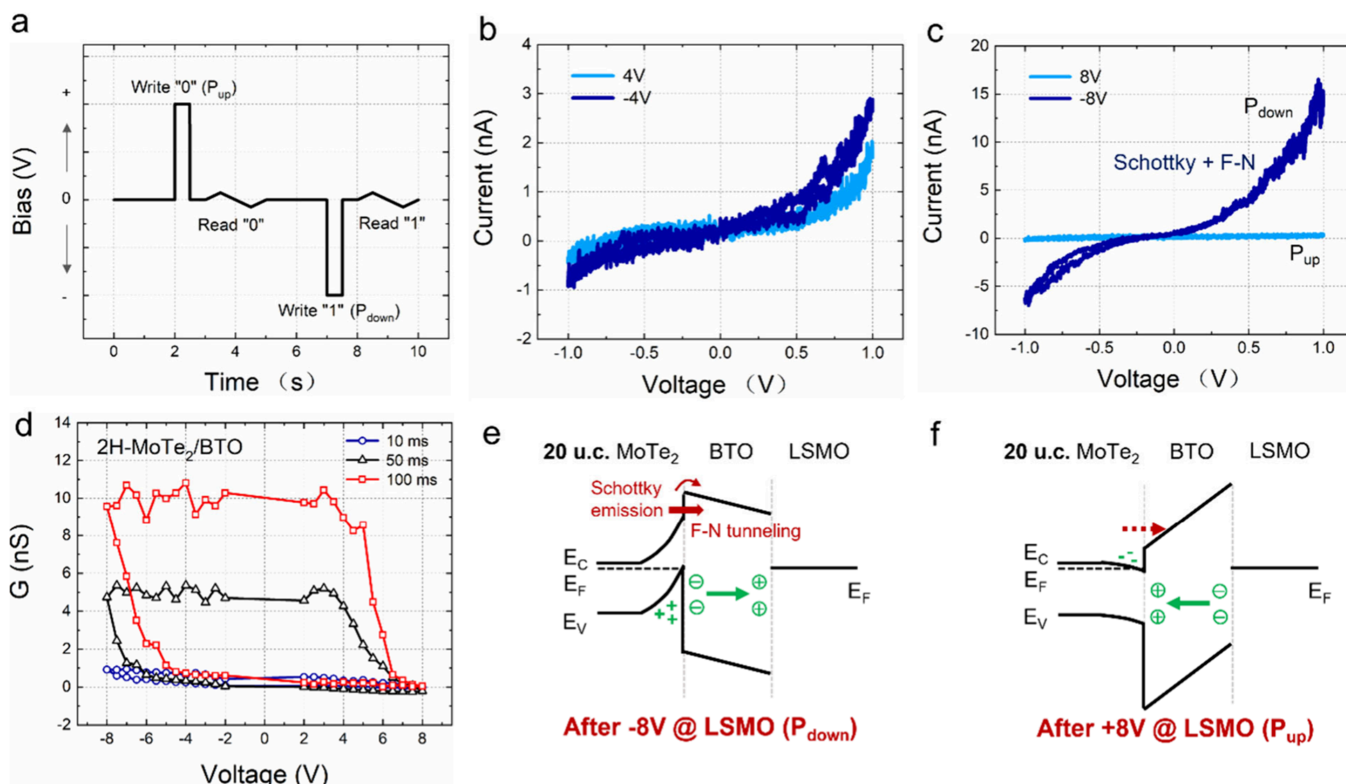


**Figure 4.** Nonvolatile memory characteristics of the 20 u.c. $MoTe_2$/BTO/LSMO heterostructure. (a) Pulse scheme for the data writing and reading processes. (b) Readout $I-V$ curves after ±4 V writing pulses. (c) Readout $I-V$ curves after ± 8 V writing pulses. (d) Conductance evolution after incremental programming pulses, demonstrating nonvolatile multilevel memory behavior. Schematics of the equilibrium state band structure after switching the BTO polarization to (e) the $P_{down}$ and (f) the $P_{up}$ states, respectively.

heterostructure exhibits more favorable band alignment and symmetric polarization switching with smaller coercive biases. Thus, its ferroelectric domain switching, electrical transport, band structure, and memory performance were further investigated. As shown in Figure S5, the ferroelectric domains in the $MoTe_2$(20 u.c.)/BTO/LSMO heterostructure can be switched using −8 V/+6 V scan bias, accompanied by corresponding changes in $V_{sp}$. The similarity between the $V_{sp}$ distribution induced by the intrinsic interface effects and by external bias indicates that interface coupling provides a deterministic and nondestructive route for polarization control.

We further investigated the electrical transport behavior of the $MoTe_2$ (20 u.c.)/BTO/LSMO heterostructure using the conductive atomic force microscope (CAFM) (Figure 3). The vertical $I-V$ loops under different sweeping biases are shown in Figure 3a. With increasing bias amplitude, the hysteresis width expands and the loop orientation reverses between clockwise and counterclockwise, indicating different interfacial states and transport mechanisms under ±3 V and ±8 V biases (Figure 3b and c). To clarify the conduction mechanisms, the $I-V$ curves were fitted by using models of trap-free space-charge-limited conduction (TF-SCLC), exponentially distributed trap SCLC (EDT-SCLC), Schottky emission, Frenkel−Poole (F−P) emission, and Fowler−Nordheim (F−N) tunneling (Section S3). Under ±3 V bias, EDT-SCLC, Schottky emission, and F−P emission dominate the on-state current, while the off-state current is primarily governed by TF-SCLC, Schottky emission, and F−P emission. These results indicate that space-charge formation at the interface controls the current flow, while trap filling leads to EDT-SCLC in the on-state. Since the polarization cannot be switched under ±3 V, the interface field determined by the band alignment dominates the transport behavior (Figure S6). Under ±8 V bias, F−N tunneling induced by the polarization field emerges, producing expanded and reversed hysteresis loops. The enhanced electric field also promotes trap filling, resulting in EDT-SCLC dominating both on- and off-state currents. The trap density, which is proportional to the critical voltage ($V_c$) marking the transition from Ohmic conduction to EDT-SCLC, is higher in the on-state due to its larger $V_c$ (Figure S7). Opposite diode responses observed under ±3 V and ±8 V biases arise from the large F−N tunneling current induced by the $P_{down}$ polarization field, which surpasses the Schottky emission contribution. In situ current mappings of the pristine state and under +6 V/−6 V bias further confirm the bidirectional transport behavior (Figure S8).

To analyze the interfacial states under different conditions, the pristine band structures governed by $W_F$ alignments and polarization field are illustrated in Figure 3d and e. The small $W_F$ difference observed between 18 u.c. $MoTe_2$ and BTO induces slight downward band bending in $MoTe_2$, leading to limited electron accumulation that stabilizes the $P_{up}$ state polarization. In contrast, the larger $W_F$ difference for 20 u.c. $MoTe_2$ produces strong upward band bending and substantial hole accumulation, stabilizing the $P_{down}$ state polarization. The $W_F$ difference between $MoTe_2$ and LSMO determines the total built-in potential ($V_{bi}$), which modulates the band bending in $MoTe_2$ and the band tilt in BTO. The excited-state band structures under external bias are shown in Figure 3f and g. The positive external bias (+3 V) applied to the LSMO layer reduces $V_{bi}$ and thus exhibits the on-state current in Figure 3b. Under +8 V bias, further reduction of $V_{bi}$ lowers the interfacial


https://doi.org/10.1021/acs.nanolett.5c05685
Nano Lett. 2026, 26, 2493−2501

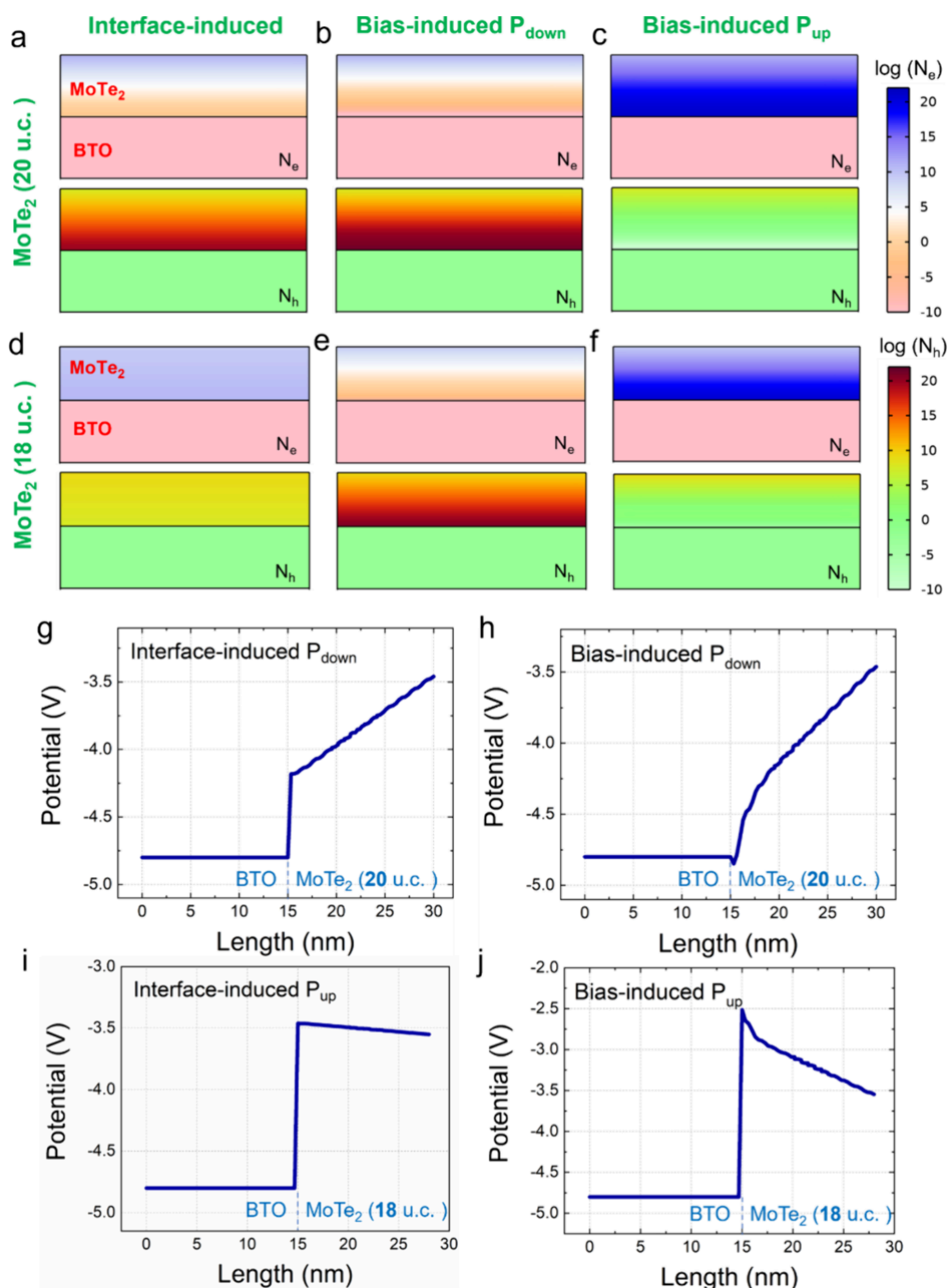


**Figure 5.** Multiphysics simulation of the interface states of the $MoTe_2$/BTO/LSMO heterostructure with different $MoTe_2$ thickness. Distribution of electron concentration ($N_e$) and hole concentration ($N_h$) of the 20 u.c. $MoTe_2$/BTO heterostructure (a) under the pristine state, (b) under the bias-induced $P_{down}$ state, and (c) under the bias-induced $P_{up}$ state, respectively. Distribution of electron concentration ($N_e$) and hole concentration ($N_h$) of the 18 u.c. $MoTe_2$/BTO heterostructure (d) under pristine state, (e) under bias-induced $P_{down}$ state, and (f) under bias-induced $P_{up}$ state, respectively. Simulated electrostatic potential line profiles of the heterostructure along the white dotted lines in Figure S12 for (g) the pristine state with 20 u.c. $MoTe_2$, (h) bias-induced $P_{down}$ state with 20 u.c. $MoTe_2$, (i) pristine state with 18 u.c. $MoTe_2$, and (j) bias-induced $P_{up}$ state with 18 u.c. $MoTe_2$, respectively.

barrier, enabling electrons accumulated at the $MoTe_2$/BTO interface to overcome or tunnel through the barrier, giving rise to a measurable current (Figure 3f). Under −8 V bias, the polarization field aligns with the contact field, generating stronger band bending and a larger $V_{bi}$ at the interface. The resulting steep upward band bending in $MoTe_2$ and band tilt in BTO trigger F−N tunneling, producing the on-state current (Figure 3g). At high biases, the EDT-SCLC contributed by the thermally excited carriers from the trap centers also contributed to the current.

Owing to its robust ferroelectric switching behavior, the $MoTe_2$/BTO/LSMO heterostructure can function as a nonvolatile memory. The data writing and reading processes are illustrated in Figure 4a. Positive (negative) pulses applied to the LSMO layer switch the polarization to the $P_{up}$ ($P_{down}$) state for data writing, and the stored state is read by a small voltage sweep. The readout characteristics after applying ±4 V and ±8 V writing pulses are shown in Figure 4b and c. A pronounced on−off ratio is obtained with ±8 V writing pulses, confirming that the polarization field strongly modulated the


https://doi.org/10.1021/acs.nanolett.5c05685
Nano Lett. 2026, 26, 2493−2501

interfacial barrier. The conduction mechanisms in the high-conductance state (Figure S9) reveal that Schottky emission and F−N tunneling jointly dominate the readout current. Beyond binary operation, multilevel storage is demonstrated by applying incremental programming pulses (Figure S10). After each pulse, conductance was read using a +1 V bias, producing conductance−voltage loops with six well-resolved memory levels and an ∼12 V memory window (Figure 4d). The on−off ratios enhance with the increase of pulse width. Figure 4e and f schematically illustrate the equilibrium band structures for the $P_{down}$ and $P_{up}$ states. The polarization field induces a substantial barrier height difference between these two states, resulting in a lower interfacial barrier and on-state current dominated by Schottky emission and F−N tunneling in the $P_{down}$ state.

To elucidate the interfacial electronic states of the $MoTe_2$/BTO/LSMO heterostructures with different $MoTe_2$ thicknesses, we analyzed the cross-sectional carrier density and electrostatic potential distributions under three representative polarization configurations: the pristine interface-induced polarization state, the bias-induced $P_{up}$ state, and the bias-induced $P_{down}$ state. These distributions were obtained using COMSOL Multiphysics simulations based on the Poisson equation and steady-state carrier transport equations (Figure 5). The employed band parameters correspond to those in Figure 2h, and the geometrical models are shown in Figure S11. BTO was modeled as an intrinsic wide-bandgap semiconductor, and the ferroelectric polarization field was incorporated via adding surface charge layers.

According to the $W_F$ difference between $MoTe_2$ (20 u.c.)/BTO and $MoTe_2$ (18 u.c.)/BTO interfaces (measured by KPFM in Figure 2c), a strong interfacial field is generated at the $MoTe_2$ (20 u.c.)/BTO interface that drives substantial hole accumulation and switches the polarization of BTO to the $P_{down}$ state (Figure 5a). In contrast, the small $W_F$ mismatch at the $MoTe_2$ (18 u.c.)/BTO interface leads to a weak interfacial field and a nearly uniform carrier distribution in $MoTe_2$, yielding a $P_{down}$ polarization state comparable to that of the bare BTO film (Figure 5d). Under the bias-induced $P_{down}$ state in the $MoTe_2$ (20 u.c.)/BTO heterostructure, the cooperative action of the ferroelectric polarization field and the large $W_F$ difference leads to pronounced electron depletion and massive hole accumulation at the $MoTe_2$/BTO interface, which results in strong interfacial hole doping in the $MoTe_2$ layer (Figure 5b). Conversely, in the $P_{up}$ state, the large polarization field induces substantial electron accumulation at the $MoTe_2$/BTO interface (Figure 5c). For the $MoTe_2$ (18 u.c.)/BTO heterostructure, the bias-induced polarization field dominates the interface states, attracting holes/electrons assembled at the $MoTe_2$/BTO interface to stabilize the $P_{down}/P_{up}$ state of BTO. Due to the thinner $MoTe_2$ layer and its associated band-structure characteristics, the carrier density in $MoTe_2$ (18 u.c.) is intrinsically lower than that of $MoTe_2$ (20 u.c.), resulting in reduced screening capability and a larger $V_c$ required for BTO polarization switching (Figure 5e and f).

To visualize the electrostatic potential and verify the band alignment, the electrostatic potential profiles are extracted along the white dashed lines in the simulated potential maps (Figure S12). Under the combined influence of the pristine $W_F$ alignment and ferroelectric polarization field, carriers accumulate at the $MoTe_2$/BTO interface, producing band tilting/bending and a potential discontinuity across the interface. For the $MoTe_2$ (20 u.c.)/BTO heterostructure, substantial hole accumulation stabilizes the $P_{down}$ polarization state, yielding a pronounced potential gradient across the $MoTe_2$ layer and a clear interface potential step at the interface (Figure 5g). Applying additional bias further enforces the $P_{down}$ state, and this downward polarization field drives even stronger hole accumulation, which further lowers the electrostatic potential (equivalently, increases the electron potential energy) at the interface (Figure 5h). In contrast, the pristine $MoTe_2$ (18 u.c.)/BTO heterostructure exhibits only a weak carrier gradient due to its small $W_F$ mismatch, producing slight electron accumulation and a subtle increase in electrostatic potential that marginally stabilizes the $P_{up}$ state (Figure 5i). Under bias-induced $P_{up}$ polarization, the upward polarization field drives substantial electron accumulation, markedly enhancing the interface electrostatic potential and stabilizing the $P_{up}$ configuration (Figure 5j). Comparison of pristine and bias-induced potential profiles reveals consistent trends, confirming that interface coupling enables deterministic and nondestructive polarization control. Moreover, the electrostatic potential profiles of the bias-induced $P_{down}$ and $P_{up}$ states clearly show that the $MoTe_2$/BTO interface barrier is reduced under the $P_{down}$ polarization state and enhanced under the $P_{up}$ state (Figure 5h and j). This polarization-controlled barrier modulation produces the large on−off ratio observed in the nonvolatile memory functionality. To rationalize these observations, the comparison of interfacial-effect-induced polarization characteristics, $V_{sp}$ difference, $W_F$ alignments, and simulated carrier and electrostatic potential distributions between $MoTe_2$ (20 u.c.)/BTO and $MoTe_2$ (18 u.c.)/BTO heterostructures is summarized in Table S1.

## 3. CONCLUSION

This work demonstrates a robust and nondestructive interfacial engineering strategy in $MoTe_2/BaTiO_3$ heterostructures by exploiting the intrinsic thickness-dependent band alignments and polarization field. By systematically combining SPM characterization and finite element simulations, we reveal that a modest two-unit-cell increase in $MoTe_2$ thickness produces a significant 0.44 eV work function shift, which inverts the interfacial doping polarity and drives ferroelectric polarization switching in the BTO layer. This discovery highlights the critical role of thickness-controlled charge redistribution in governing ferroelectric switching behavior. Thicker $MoTe_2$ layers (>20 u.c.) provide enhanced interfacial screening and favorable band alignment, enabling symmetric and low-bias polarization switching. Thinner $MoTe_2$ layers (<18 u.c.) exhibit asymmetric switching with a higher energy barrier. Electrical-transport analyses further reveal a bias-driven transition from trap-mediated SCLC and thermionic emission to F−N tunneling under a strong ferroelectric polarization field, supporting reliable nonvolatile memory operation. Collectively, these findings establish a new paradigm for interface-driven device design, demonstrating that atomic-scale thickness engineering can precisely tailor electronic structure and ferroelectric switching dynamics. Beyond the $MoTe_2$/BTO system, this strategy is broadly applicable to other 2D/ferroelectric platforms.

## ■ ASSOCIATED CONTENT

### Supporting Information

The Supporting Information is available free of charge at https://pubs.acs.org/doi/10.1021/acs.nanolett.5c05685.


https://doi.org/10.1021/acs.nanolett.5c05685
Nano Lett. 2026, 26, 2493−2501

Experimental section; ferroelectric characteristics of the $MoTe_2$/BTO heterostructure; electrical transport behavior of the $MoTe_2$/BTO heterostructure; memory behavior of the $MoTe_2$/BTO heterostructure; interface states of the $MoTe_2$/BTO heterostructure (PDF)

## AUTHOR INFORMATION

### Corresponding Authors

**Ming Xu** − *School of Optoelectronic Science and Intelligent Instrumentation & Shaanxi University Key Laboratory of Photonic Power Devices and Discharge Regulation, Xi'an University of Technology, Xi'an 710048, China;* orcid.org/0000-0002-1953-2723; Email: xuming@xaut.edu.cn

**Tao Li** − *Center for Spintronics and Quantum Systems, State Key Laboratory for Mechanical Behavior of Materials, Department of Materials Science and Engineering, Xi'an Jiaotong University, Xi'an 710049, China;* orcid.org/0009-0008-6820-3863; Email: taoli66@xjtu.edu.cn

### Authors

**Yuqing Zhou** − *School of Optoelectronic Science and Intelligent Instrumentation & Shaanxi University Key Laboratory of Photonic Power Devices and Discharge Regulation, Xi'an University of Technology, Xi'an 710048, China;* orcid.org/0000-0001-7986-5338

**Feiyan Hou** − *Center for Spintronics and Quantum Systems, State Key Laboratory for Mechanical Behavior of Materials, Department of Materials Science and Engineering, Xi'an Jiaotong University, Xi'an 710049, China;* orcid.org/0000-0001-7019-5366

**Xingke Fu** − *Beijing National Laboratory for Condensed Matter Physics, Institute of Physics, Chinese Academy of Sciences, Beijing 100190, China*

**Chen Ge** − *Beijing National Laboratory for Condensed Matter Physics, Institute of Physics, Chinese Academy of Sciences, Beijing 100190, China;* orcid.org/0000-0002-8093-940X

**Kaiming Wang** − *School of Optoelectronic Science and Intelligent Instrumentation & Shaanxi University Key Laboratory of Photonic Power Devices and Discharge Regulation, Xi'an University of Technology, Xi'an 710048, China;* orcid.org/0000-0002-7564-8712

**Siqing Zhang** − *School of Optoelectronic Science and Intelligent Instrumentation & Shaanxi University Key Laboratory of Photonic Power Devices and Discharge Regulation, Xi'an University of Technology, Xi'an 710048, China*

**Jianpei Xing** − *School of Optoelectronic Science and Intelligent Instrumentation & Shaanxi University Key Laboratory of Photonic Power Devices and Discharge Regulation, Xi'an University of Technology, Xi'an 710048, China*

**Li Sun** − *School of Optoelectronic Science and Intelligent Instrumentation & Shaanxi University Key Laboratory of Photonic Power Devices and Discharge Regulation, Xi'an University of Technology, Xi'an 710048, China*

**Ruidong Lv** − *School of Optoelectronic Science and Intelligent Instrumentation & Shaanxi University Key Laboratory of Photonic Power Devices and Discharge Regulation, Xi'an University of Technology, Xi'an 710048, China*

**Qian Liu** − *School of Optoelectronic Science and Intelligent Instrumentation & Shaanxi University Key Laboratory of Photonic Power Devices and Discharge Regulation, Xi'an University of Technology, Xi'an 710048, China*

**Fengjuan Wang** − *School of Automation and Information Engineering & Shaanxi University Key Laboratory of Photonic Power Devices and Discharge Regulation, Xi'an University of Technology, Xi'an 710048, China*

**Kaiyang Zeng** − *Department of Mechanical Engineering, National University of Singapore, Singapore 117576, Singapore;* orcid.org/0000-0002-3348-0018

**Tai Min** − *Center for Spintronics and Quantum Systems, State Key Laboratory for Mechanical Behavior of Materials, Department of Materials Science and Engineering, Xi'an Jiaotong University, Xi'an 710049, China; School of Advanced Manufacturing Engineering, Nanjing University, Suzhou 215163, China; State Key Laboratory of Solid State Microstructures, Nanjing University, Nanjing 210093, China*

Complete contact information is available at: https://pubs.acs.org/10.1021/acs.nanolett.5c05685

### Author Contributions

T.L. and Y.Z. conceived the experimental ideas. Y.Z. prepared the heterostructure, carried out the PFM, KPFM, and CAFM tests, performed the multiphysics simulations, and analyzed the data under the guidance of T.L., M.X., K.Z., and T.M. X.F. and C.G. prepared the BTO substrates. F.H. helped to analyze the data. Y.Z. wrote the manuscript. All the coauthors participated in the discussion and provided their inputs to the paper.

### Notes

The authors declare no competing financial interest.

## ACKNOWLEDGMENTS

This work was financially supported by the National Key Research and Development Program of China (Grant No. 2021YFA1202200), the National Natural Science Foundation of China (Grant Nos. 51802250, 12222414, 12074416), Scientific Research Program Funded by Shaanxi Provincial Education Department (Program No. 25JK0575), Young Talent Fund of Association for Science and Technology in Shaanxi, China (No. 20250517), and the Youth Innovation Promotion Association of Chinese Academy of Science (No. Y2022003). Y.Z. acknowledges the financial support from the China Scholarship Council (No. 202206280109).

## REFERENCES

(1) Uzhansky, M.; Mukherjee, S.; Vijayan, G.; Koren, E. Non-volatile reconfigurable p−n junction utilizing in-plane ferroelectricity in 2D WSe2/α-In2Se3 asymmetric heterostructures. *Adv. Funct. Mater.* **2024**, *34* (8), 2306682.

(2) Zhang, H.; Fu, J.; Carvalho, A.; Poh, E. T.; Chung, J. Y.; Feng, M.; Chen, Y.; Wang, B.; Shang, Q.; Yang, H.; et al. Programmable interfacial band configuration in WS2/Bi2O2Se heterojunctions. *ACS Nano* **2024**, *18* (26), 16832−16841.

(3) Wang, Z.; Liu, X.; Zhou, X.; Yuan, Y.; Zhou, K.; Zhang, D.; Luo, H.; Sun, J. Reconfigurable quasi-nonvolatile memory/subthermionic fet functions in ferroelectric-2D semiconductor vdw architectures. *Adv. Mater.* **2022**, *34* (15), 2200032.

(4) Lu, Y.; Xie, D.; Zhang, C.; Cao, D.; Chen, X.; Shu, H. Band alignment engineering in 2D ferroelectric van der waals heterostructures for all-in-one optoelectronic architecture. *Adv. Electron. Mater.* **2025**, *11* (2), 2400269.

(5) Sun, X.; Chen, Y.; Zhao, D.; Taniguchi, T.; Watanabe, K.; Wang, J.; Xue, J. Measuring band modulation of MoS2 with ferroelectric gates. *Nano Lett.* **2023**, *23* (6), 2114−2120.

(6) Wang, X.; Yasuda, K.; Zhang, Y.; Liu, S.; Watanabe, K.; Taniguchi, T.; Hone, J.; Fu, L.; Jarillo-Herrero, P. Interfacial ferroelectricity in rhombohedral-stacked bilayer transition metal dichalcogenides. *Nat. Nanotechnol.* **2022**, *17* (4), 367−371.

(7) Van Winkle, M.; Dowlatshahi, N.; Khaloo, N.; Iyer, M.; Craig, I. M.; Dhall, R.; Taniguchi, T.; Watanabe, K.; Bediako, D. K. Engineering interfacial polarization switching in van der Waals multilayers. *Nat. Nanotechnol.* **2024**, *19* (6), 751−757.

(8) Gao, Y.; Weston, A.; Enaldiev, V.; Li, X.; Wang, W.; Nunn, J. E.; Soltero, I.; Castanon, E. G.; Carl, A.; De Latour, H.; et al. Tunnel junctions based on interfacial two dimensional ferroelectrics. *Nat. Commun.* **2024**, *15* (1), 4449.

(9) Kang, K.; Zhao, W.; Zeng, Y.; Watanabe, K.; Taniguchi, T.; Shan, J.; Mak, K. F. Switchable moiré potentials in ferroelectric WTe2/WSe2 superlattices. *Nat. Nanotechnol.* **2023**, *18* (8), 861−866.

(10) Wang, H.; Tang, Y.; Wang, Z.; He, C.; Liu, H.; Lin, R.; Xu, W.; Chen, J.; Wang, S.; Yan, X. Efficient and stable topological/ferroelectric Bi2Te3/SnSe hetero-memristor for in situ bionic-visual semi-hardware systems. *Adv. Mater.* **2025**, *37* (35), 2501066.

(11) Feng, Y. P.; Wang, Y. J.; Tang, Y. L.; Zhu, Y. L.; Ma, X. L. Interfacial manipulation of polar topologies in oxide ferroelectric films. *Adv. Funct. Mater.* **2025**, *35*, No. e10402.

(12) Yadav, A. K.; Nelson, C. T.; Hsu, S. L.; Hong, Z.; Clarkson, J. D.; Schlepütz, C. M.; Damodaran, A. R.; Shafer, P.; Arenholz, E.; Dedon, L. R.; et al. Observation of polar vortices in oxide superlattices. *Nature* **2016**, *530* (7589), 198−201.

(13) Zubko, P.; Wojdeł, J. C.; Hadjimichael, M.; Fernandez-Pena, S.; Sené, A.; Luk'yanchuk, I.; Triscone, J. M.; Íñiguez, J. Negative capacitance in multidomain ferroelectric superlattices. *Nature* **2016**, *534* (7608), 524−528.

(14) Singh, S.; Kim, K. H.; Jo, K.; Musavigharavi, P.; Kim, B.; Zheng, J.; Trainor, N.; Chen, C.; Redwing, J. M.; Stach, E. A.; et al. Nonvolatile control of valley polarized emission in 2D WSe2-AlScN heterostructures. *ACS Nano* **2024**, *18* (27), 17958−17968.

(15) Zhai, B.; Cheng, R.; Yao, W.; Yin, L.; Shen, C.; Xia, C.; He, J. Using ferroelectric polarization to regulate and preserve the valley polarization in a HfN2/CrI3/In2Se3 heterotrilayer. *Phys. Rev. B* **2021**, *103* (21), 214114.

(16) Xun, W.; Wu, C.; Sun, H.; Zhang, W.; Wu, Y. Z.; Li, P. Coexisting magnetism, ferroelectric, and ferrovalley multiferroic in stacking-dependent two-dimensional materials. *Nano Lett.* **2024**, *24* (11), 3541−3547.

(17) Pucher, T.; Puebla, S.; Zamora, V.; Sánchez Viso, E.; Rouco, V.; Leon, C.; Garcia Hernandez, M.; Santamaria, J.; Munuera, C.; Castellanos Gomez, A. Strong electrostatic control of excitonic features in MoS2 by a free-standing ultrahigh-$\kappa$ ferroelectric perovskite. *Adv. Funct. Mater.* **2024**, *34* (52), 2409447.

(18) Ramirez, M. O.; Fernandez Tejedor, J.; Gallego, D.; Fernández Martinez, J.; Molina, P.; Hernández Pinilla, D.; Gómez Herrero, J.; Ares, P.; Bausá, L. E. Light-induced ferroelectric modulation of p-n homojunctions in monolayer MoS2. *Adv. Opt. Mater.* **2024**, *12* (21), 2400624.

(19) Zhou, C.; Feng, Y.; Ma, L.; Huang, H.; Si, Y.; Wang, H.; Huang, S.; Li, J.; Kuo, C. Y.; Das, S.; et al. Fatigue-free ferroelectricity in Hf0.5Zr0.5O2 ultrathin films via interfacial design. *Nat. Commun.* **2025**, *16* (1), 7593.

(20) Wu, J.; Chen, H. Y.; Yang, N.; Cao, J.; Yan, X.; Liu, F.; Sun, Q.; Ling, X.; Guo, J.; Wang, H. High tunnelling electroresistance in a ferroelectric van der Waals heterojunction via giant barrier height modulation. *Nat. Electron.* **2020**, *3* (8), 466−472.

(21) Gao, J.; Lian, X.; Chen, Z.; Shi, S.; Li, E.; Wang, Y.; Jin, T.; Chen, H.; Liu, L.; Chen, J.; et al. Multifunctional MoTe2 Fe-FET enabled by ferroelectric polarization-assisted charge trapping. *Adv. Funct. Mater.* **2022**, *32* (17), 2110415.

(22) Xu, H.; Sun, F.; Li, E.; Guo, W.; Hua, L.; Wang, R.; Li, W.; Chu, J.; Liu, W.; Luo, J.; et al. Ferroelectric perovskite/MoS2 channel heterojunctions for wide-window nonvolatile memory and neuromorphic computing. *Adv. Mater.* **2025**, *37* (4), 2414339.

(23) Zhou, Y.; Zeng, Q.; Fu, X.; Yang, C.; Hou, F.; Ge, C.; Zeng, K.; Liu, H.; Chai, Z.; Min, T.; et al. An interface-engineered three-channel synapse using staggered transition metal dichalcogenides/ferroelectric heterojunctions. *Chem. Eng. J.* **2025**, *526*, 171003.

(24) Wang, B.; Chen, W.; Zou, L.; Wang, T.; Li, Z.; Wang, Z.; Xu, H.; Xu, L.; Lan, S.; Feng, P.; et al. A programmable nonvolatile schottky diode based on van der waals ferroelectric junction. *Nano Lett.* **2025**, *25* (26), 10699−10708.

(25) Chen, Y.; Wang, X.; Huang, L.; Wang, X.; Jiang, W.; Wang, Z.; Wang, P.; Wu, B.; Lin, T.; Shen, H.; et al. Ferroelectric-tuned van der Waals heterojunction with band alignment evolution. *Nat. Commun.* **2021**, *12* (1), 4030.

(26) She, J.; Liu, X.; Liu, H.; Yu, H.; Wang, J.; Shen, Z.; Xiao, B.; Cheng, Y.; Yin, Z.; Meng, G. Ferroelectric tailorable WS2/Graphene phototransistors. *Nano Lett.* **2025**, *25* (30), 11578−11585.

(27) Li, D.; Huang, X.; Xiao, Z.; Chen, H.; Zhang, L.; Hao, Y.; Song, J.; Shao, D. F.; Tsymbal, E. Y.; Lu, Y.; et al. Polar coupling enabled nonlinear optical filtering at MoS2/ferroelectric heterointerfaces. *Nat. Commun.* **2020**, *11* (1), 1422.

(28) Jeong, Y.; Tordi, P.; Tamayo, A.; Han, B.; Bonini, M.; Samorì, P. Mimicking Synaptic Plasticity: Optoionic MoS2 memory powered by biopolymer hydrogels as a dynamic cations reservoir. *Adv. Funct. Mater.* **2025**, *35*, No. e09607.

(29) Li, T.; Sharma, P.; Lipatov, A.; Lee, H.; Lee, J. W.; Zhuravlev, M. Y.; Paudel, T. R.; Genenko, Y. A.; Eom, C. B.; Tsymbal, E. Y.; et al. Polarization-mediated modulation of electronic and transport properties of hybrid MoS2-BaTiO3-SrRuO3 tunnel junctions. *Nano Lett.* **2017**, *17* (2), 922−927.

(30) Lee, J.; Duong, N. T.; Bang, S.; Park, C.; Nguyen, D. A.; Jeon, H.; Jang, J.; Oh, H. M.; Jeong, M. S. Modulation of junction modes in SnSe2/MoTe2 broken-Gap van der Waals heterostructure for multifunctional devices. *Nano Lett.* **2020**, *20* (4), 2370−2377.

(31) Li, W.; Guo, Y.; Luo, Z.; Wu, S.; Han, B.; Hu, W.; You, L.; Watanabe, K.; Taniguchi, T.; Alava, T.; et al. A gate programmable van der Waals metal-ferroelectric-semiconductor vertical heterojunction memory. *Adv. Mater.* **2023**, *35* (5), 2208266.

(32) Kim, H. G.; Choi, H. J. Thickness dependence of work function, ionization energy, and electron affinity of Mo and W dichalcogenides from DFT and GW calculations. *Phys. Rev. B* **2021**, *103* (8), 085404.

(33) Pandey, S. K.; Das, R.; Mahadevan, P. Layer-dependent electronic structure changes in transition metal dichalcogenides: the microscopic origin. *ACS Omega* **2020**, *5* (25), 15169−15176.

(34) Momeni, K.; Ji, Y.; Wang, Y.; Paul, S.; Neshani, S.; Yilmaz, D. E.; Shin, Y. K.; Zhang, D.; Jiang, J. W.; Park, H. S.; et al. Multiscale computational understanding and growth of 2D materials: a review. *Npj Comput. Mater.* **2020**, *6* (1), 22.

(35) Cho, Y.; Park, J. H.; Kim, M.; Jeong, Y.; Ahn, J.; Kim, T.; Choi, H.; Yi, Y.; Im, S. Fully transparent p-MoTe2 2D transistors using ultrathin MoOx/Pt contact media for indium-tin-oxide source/drain. *Adv. Funct. Mater.* **2018**, *28* (39), 1801204.

(36) Zhou, Y.; Yang, C.; Fu, X.; Liu, Y.; Yang, Y.; Wu, Y.; Ge, C.; Min, T.; Zeng, K.; Li, T. Optical modulation of MoTe2/Ferroelectric heterostructure via interface doping. *ACS Appl. Mater. Interfaces* **2024**, *16* (10), 13247−13257.

(37) De Jong, M. P.; Dediu, V. A.; Taliani, C.; Salaneck, W. R. Electronic structure of La0.7Sr0.3MnO3 thin films for hybrid organic/inorganic spintronics applications. *J. Appl. Phys.* **2003**, *94* (11), 7292−7296.




https://doi.org/10.1021/acs.nanolett.5c05685
Nano Lett. 2026, 26, 2493−2501